Journal of Alloys and Compounds 936 (2023) 168348

Contents lists available at ScienceDirect

Journal of Alloys and Compounds

journal homepage: www.elsevier.com/locate/jalcom

Magnetic and crystal structure of the antiferromagnetic skyrmion candidate $GdSb_{0.71}Te_{1.22}$

Igor Plokhikh [a,*], Oscar Fabelo [b], Lilian Prodan [c,d], Michael Wörle [e], Ekaterina Pomjakushina [a], Antonio Cervellino [f], Vladimir Tsurkan [c,d], István Kézsmárki [d], Oksana Zaharko [g]

[a] Laboratory for Multiscale Materials Experiments, Paul Scherrer Institut, PSI, Villigen, CH-5232, Switzerland
[b] Institut Laue-Langevin, 71 Avenue des Martyrs, 38000 Grenoble, France
[c] Institute of Applied Physics, Chisinau, Moldova
[d] Experimental Physics V, University of Augsburg, 86135 Augsburg, Germany
[e] Laboratorium für Anorganische Chemie, ETH Zürich, CH-8093 Zürich, Switzerland
[f] Swiss Light Source, Paul Scherrer Institute, CH-5232 Villigen, Switzerland
[g] Laboratory for Neutron Scattering and Imaging, Paul Scherrer Institut, PSI, Villigen, CH-5232, Switzerland

ARTICLE INFO

Article history:
Received 23 August 2022
Received in revised form 8 November 2022
Accepted 1 December 2022
Available online 5 December 2022

Keywords:
Skyrmion
Hot-neutron diffraction
Topological semimetals

ABSTRACT

$GdSb_{0.46}Te_{1.48}$, a nonsymmorphic Dirac semimetal with Dirac nodes at the Fermi level, has a rich magnetic phase diagram with one of the phases predicted to be an antiferromagnetic skyrmion state. In the current work, we investigate $GdSb_{0.71}Te_{1.22}$ through bulk magnetization measurements, single-crystal, and powder synchrotron X-ray diffraction, as well as single-crystal hot-neutron diffraction. We resolve a weak orthorhombic distortion with respect to the tetragonal structure and charge density wave (CDW) satellites due to incommensurate modulations of the crystal structure. At 2 K the magnetic structure is modulated with two propagation vectors, k_I = (0.45 0 0.45) and k_{II} = (0.4 0 0), with all their arms visible. While k_I persists up to the transition to the paramagnetic state at T_N = 11.9 K, k_{II} disappears above an intermediate magnetic transition at T_1 = 5 K. Whereas magnetic field applied along the *c*-axis has only a weak effect on the intensity of antiferromagnetic reflections, it is effective in inducing an additional ferromagnetic component on Gd atoms. We refine possible magnetic structures of $GdSb_{0.71}Te_{1.22}$ and discuss the possibility of hosting magnetic textures with non-trivial 3D+ 2 topologies in the $GdSb_{1-x}Te_{1+x}$ series.

1. Introduction

Topology concepts in solid-state science [1–3] have revived interest in frustrated magnets, as intriguing topological phenomena can appear both below and above the long-range magnetic ordering. Furthermore, materials hosting skyrmions, mesoscale topological spin textures, attract a significant interest due to their high potential in spintronics, e.g., in next-generation memory devices [4–8]. In addition to the non-trivial topology of such spin textures in real space, topological features in the electronic band structure, such as Dirac or Weil nodes, may predispose useful technological properties like large magnetoresistance and high charge carrier mobility [1–3].

In most skyrmion-host crystals, the thermal stability range of the skyrmion lattice state is rather limited, as this phase is stabilized only under a specific combination of the micro- and macroscopic parameters. This applies to centrosymmetric systems with frustrated exchange interactions and also to non-centrosymmetric crystals, where the competition between the Dzyaloshinskii-Moriya interaction and Heisenberg exchange leads to the formation of skyrmions. Since strong magnetic anisotropy, comparable to the leading exchange interactions, generally favours collinear magnetic structures in bulk crystals, weak magnetic anisotropy is a key factor to promote the formation of multi-*k* magnetic lattices with non-trivial topology [9–13]. From this perspective, the compounds containing ions with half-filled 3*d* of 4*f* shells are promising candidates. Indeed, some examples of Mn^{2+} ($3d^5$) and Gd^{3+} ($4f^7$) materials that host skyrmions are extensively discussed in literature, including $GdRu_2Si_2$ [14], Gd_2PdSi_3 [15], Mn_3Sn [16], MnSi [17], and $MnSc_2S_4$ [18].

This study was motivated by the recent proposal of an antiferromagnetic skyrmion lattice in $GdSb_{0.46}Te_{1.48}$ based on magnetization and magnetocaloric measurements [19]. The more general class, the *Ln*SbTe compounds (*Ln* = lanthanide) belong to the ZrSiS (PbFCl)-structure type and, similarly to the prototype, are Dirac nodal-line semimetals [20–24]. Substantial structural flexibility, the

* Corresponding author.
E-mail address: igor.plokhikh@psi.ch (I. Plokhikh).

https://doi.org/10.1016/j.jallcom.2022.168348

presence of magnetic lanthanide ions, and topological electronic structure make this material family a useful platform to study the interplay between structural, electronic and magnetic instabilities. Although the crystal structure and the basic physical properties have not been reported for all lanthanide members of the *Ln*SbTe family, two particular members (CeSbTe and GdSbTe) merit an extensive discussion in the literature owing to their intriguing physics. For example, degeneracy in the electronic structure of CeSbTe can be lifted by breaking the time-reversal symmetry using a small field in the sub-Tesla range [25]. This evolves into a peculiar multi-stage process through a partial substitution of Sb by Te [26] owing to interplay between the magnetic and charge orders.

By substituting Sb by Te in GdSbTe, one can obtain a series of solid solutions $GdSb_{1-x}Te_{1+x}$ that, depending on the exact value of *x*, features different CDW superstructures of the parent cell [19,27–29]. At low *x* (below *ca.* 0.2), the crystal preserves the initial tetragonal structure, while at higher values, it undergoes an orthorhombic distortion accompanied by the evolution of complex CDW superstructure and accumulation of vacancies in the Sb/Te net. By virtue of chemical pressure, such substitution affects the electronic structure – the intermediate phase with the composition $GdSb_{0.46}Te_{1.48}$ provides a close realization of Dirac nodes at the Fermi level. Hereafter, we will refer to this compound as GST. The compounds around this composition show a rich and complex magnetic phase diagram with three transitions in zero field and several field-induced phases. Magnetization measurements hint at a skyrmion phase in this material in a small critical region, extending over the temperature range of 6.2 – 7 K and the field range of 0 – 0.3 T [19]. Given the fundamental and potential practical importance of skyrmions, these compounds deserve a more detailed microscopic study.

Neutron diffraction is a conventional method to elucidate magnetic ordering on a microscopic level and to follow the evolution of the magnetic structure with external parameters, like magnetic field and temperature. However, the strong neutron absorption of the natural Gd precludes routine neutron studies of its compounds. In the present report, we overcome this limitation using hot neutrons (0.5 Å, *ca.* 330 meV), where absorption is substantially mitigated [30]. We show that the ground state magnetic structure features two incommensurate propagation vectors that are not related by symmetry. We also discuss the possible formation of topologically nontrivial magnetic structures based on our data.

2. Experimental part

The single crystals have been grown by the chemical vapour transport reaction from the preliminary synthesized polycrystalline material with an appropriate ratio of Sb to Te and iodine as a transport agent [19,27–29]. The polycrystalline samples were obtained by solid-state reaction from high-purity elements. All consequent measurements were done on the samples extracted from the same batch. The phase analysis was performed using conventional X-ray powder diffraction. The composition of the crystals was analyzed by ZEISS Crossbeam 550, using energy dispersive x-ray spectroscopy (EDS). Magnetic susceptibility was measured by a SQUID magnetometer (MPMS 3, Quantum Design) in magnetic fields up to 5 T.

Hot neutron single-crystal diffraction has been performed on the D9 diffractometer at ILL [31]. The crystals were glued into an aluminium pin, attached to a goniometer, and loaded either in a 4-circle He-flow cryostat (for collecting the zero-field data) or into a cryomagnet (for applied field studies). A small two-dimensional (2D) area detector of 6 × 6 cm (32 × 32 pixels) allows reciprocal space survey, optimizing the nuclear peak position, and searching for incommensurate magnetic reflections. The program RACER [32] was used to integrate the omega- and omega-2theta-scans and to correct them for the Lorentz factor. Long q-scans were collected along specific directions to assess the presence of the different propagation vectors. Reciprocal space survey was done using the Int3D program [33]. The neutron wavelength was set to 0.5 Å to minimize the absorption due to the presence of natural gadolinium in the sample. The raw diffraction data are available at the ILL data depository [34].

Variable temperature synchrotron powder X-ray diffraction has been collected at MS - X04SA: Materials Science beamline at SLS (PSI) at 0.49235 Å (25 keV) [35]. Single-crystal X-ray diffraction datasets were collected using Bruker SMART Platform diffractometer with Apex I CCD-Detector (MoKα radiation) at room temperature and at 100 K. Data reduction was done with Rigaku CrysAlisPro 1.171.40.67a [36].

Diffraction data were treated using JANA2006/JANA2020 software [37,38]. Representation/magnetic symmetry analysis [39] has been performed using ISODISTORT online tool [40,41]. The magnetic structures were plotted using VESTA [42].

3. Results and discussion

3.1. X-ray diffraction

X-ray powder diffraction confirms orthorhombic symmetry of the studied crystals; all strong reflections can be indexed in the *Pmmn* unit cell *a* = 4.2861(2) Å, *b* = 4.3257(2) Å, *c* = 9.1183(3) Å. On the other hand, single-crystal X-ray diffraction shows effectively tetragonal structure due to the ferroelastic twinning. Pronounced CDW atomic superstructure, associated with the incommensurate vector k_a = (0.172 0 0) due to small displacements of atoms from the ideal average position, is evident. Crystal structure refinement reveals the presence of vacancies in the mixed Sb/Te position consistent with the composition $GdSb_{0.71}Te_{1.22}$ derived from EDS measurements. A more detailed description is provided in SI.

3.2. Magnetic properties

The temperature-dependent magnetic susceptibility of a $GdSb_{0.71}Te_{1.22}$ crystal was measured in various fields applied along the *c*-axis, as shown in Fig. 1. The compound undergoes an antiferromagnetic transition at T_N = 11.9 K, which is only slightly reduced with increasing magnetic field. In low fields, susceptibility curves exhibit two other transitions at, T_1 = 5 K and T_2 = 6.9 K. In finite magnetic fields, T_1 and T_2 converge to each other, and above *ca.* 2 T they are merged into a single transition. T_1, T_2, and T_N separate three magnetically ordered phases marked as AFM1 $T < T_1$, AFM2 $T_1 < T < T_2$ and AFM3 $T_2 < T < T_N$, according to the notation in Ref.

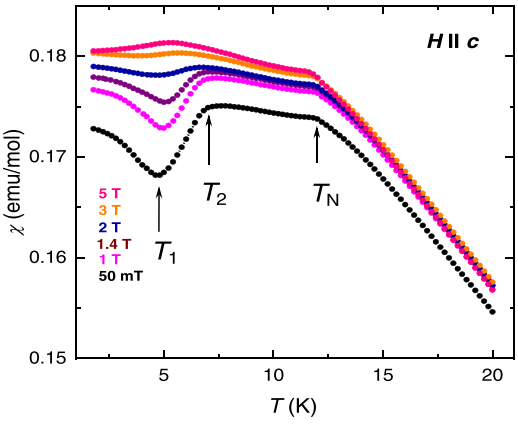

Fig. 1. Magnetic susceptibility *vs* temperature measured in different fields applied along the *c*-axis. Three anomalies, observed at T_1, T_2, and T_N, indicate magnetic transitions.

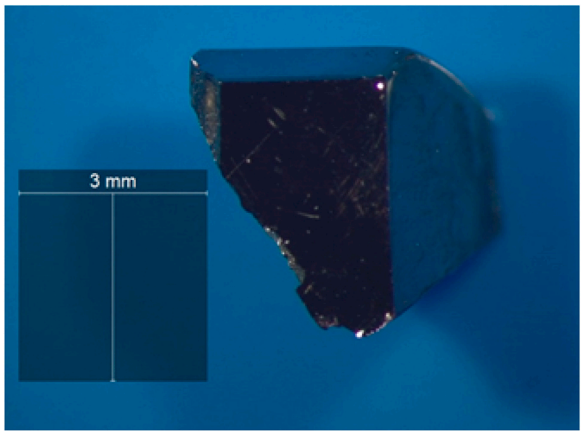

Fig. 2.. Crystal $GdSb_{0.71}Te_{1.22}$ of mass of *ca.* 300 mg used for hot neutron single-crystal diffraction study in a cryomagnet on the D9 instrument at ILL.

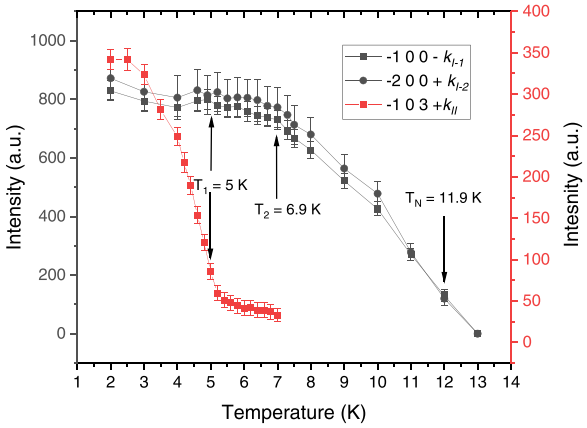

Fig. 3.. Temperature dependences of selected magnetic reflections of k_I and k_{II} in zero field for the big crystal shown in Fig. 2. The temperatures of phase transitions from the *magnetization measurements* are outlined. Note, that whereas k_{II} reflections were measured in the Displex cryostat, the k_I ones were measured in cryomagnet, which leads to larger error bars (see explanations in the text).

[19]. The magnetic susceptibility curves measured for our crystals are qualitatively similar to those shown in literature, with two major exceptions. The transition temperatures (T_N = 11.9 K, T_2 = 6.9 K, and T_1 = 5 K) are slightly lower than those reported earlier (13.2 K, 8.5 K, and 7.2 K, respectively). In addition, slightly below T_1, the low-field magnetization data in Ref. [19] show a sharp upturn, which is not present in our crystals.

3.3. Single-crystal hot-neutron diffraction

The *small crystal* (brick-shaped, *ca.* 0.7 ×1.5 ×1.8 mm) was studied in zero-field in a Displex cryostat, while the *big one* shown in Fig. 2 was studied both in cryomagnet and Displex cryostat. Using a bigger crystal in the cryomagnet was crucial as the more massive sample environment creates significant background.

The room temperature ND dataset is consistent with the X-ray data, *i.e.* we observe an effectively tetragonal crystal structure. No superstructure reflections were observed due to their low intensities. Attempts to fit the measured intensities to the X-ray model using tabulated values of nuclear neutron scattering factors [43] yield poor residuals. This is because, whereas the scattering factors are tabulated for the 1.8 Å neutrons, the natural Gd has a very strong energy dependence close to the thermal region due to the resonant effects in the ^{155}Gd and ^{157}Gd isotopes [44,45]. For neutrons with λ = 1.8 Å, the real part of the nuclear scattering factor is 6.5 fm and the imaginary is − 13.82 fm, whereas at 0.5 Å is *c.a.* 11 fm and − 0.5 fm, respectively. Plugging the 0.5 Å scattering length of Gd into refinement yields good agreement factors even *without* absorption correction (R_I = 7.6 %, R_{WI} = 9.1 %, χ^2 = 1.9 for 145 independent reflections and 13 refined parameters). To improve the fit, we performed a series of refinements with numerical shape-corrected absorption and variable absorption coefficient. The R_{int} (the factor indicating agreement between the equivalent reflections) has the lowest value for $\mu \sim 0.35\ mm^{-1}$, which is in good agreement with the literature [30] value of $0.66\ mm^{-1}$ and was used for correction of magnetic intensities (*vide infra*). The estimated absorption coefficient yields transmission T_{min}/T_{max} of 55 %/68 % and lowers the residuals to R_F = 5.3 %, R_{WF} = 6.6 %, χ^2 = 1.2.

Besides the nuclear reflections, the neutron diffraction pattern collected at 2 K exhibits a set of additional reflections. They disappear upon heating to 15 K (> T_N), and thus are of magnetic origin. The majority of strong magnetic reflections can be indexed using the propagation vector k_I = (0.45 0 0.45), whereas there are other small ones corresponding to k_{II} = (0.4 0 0). Reflections belonging to all arms of k_I and k_{II} are visible. No nuclear reflections gain intensity in zero-field in the magnetically ordered state, hence the k = 0 component can be ruled out. Temperature-dependent intensities for selected reflections corresponding to k_I and k_{II} are shown in Fig. 3. The k_{II} reflection exists between 2 K and T_1, and is gone at higher temperatures, while the k_I reflections are present in the whole range between 2 K and T_N.

Topologically non-trivial magnetic phases sought-for in the title material should be based on several propagation vectors, *i.e.,* represent so-called multi-*k* structures. Distinguishing them from single-*k* structures is not trivial. The most reliable way to establish relations between different vectors (k_I and k_{II}, in our case) as well as between their arm/domains is by applying an external stimulus, like magnetic field, which can change the magnetic structure and/or domain population. In our experiment the high background originating from the cryomagnet precludes reliable measurements of weak reflections. This was fatal for the k_{II} reflections, as they could not be probed in the part of reciprocal space accessible in the cryomagnet. Still it is clear that k_I and k_{II} originate from different phases existing in the crystal, due to different temperature dependences of their intensities in zero field. We do not observe evolving k_I-k_I cross-satellites in applied field. The intensities of different arms of k_I are nearly field-independent (Fig. 4). Hence, our in-field studies are not conclusive enough to distinguish between the multi-domain and multi-*k* scenarios for the k_I vector.

The effect of the field on magnetic intensities is the most prominent for the (110) main reflection, but not for the (111) one, field dependences of which are provided in Fig. S6. At 6 K, the (110) intensity grows in the field up to 1 T after, followed by a drop and

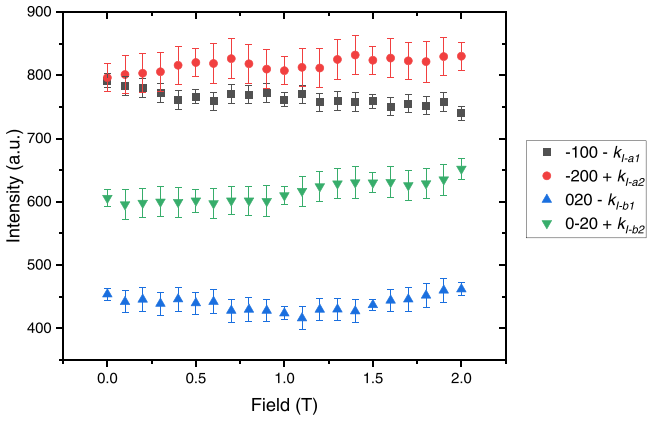

Fig. 4. Field dependence for the selected reflections of k_I belonging to the different arms at 6 K.

Gd	*x*	*y*	*z*
sin	1.9(5)	3.7(1)	0
cos	0.9(6)	4.7(1)	0

Fig. 5. Details of the magnetic structure corresponding to k_I – schematic representation of the structure and (*x, y, z*) components of the magnetic wave.

resuming the growth at *ca.* 1.5 T. This is consistent with the field-induced magnetic moment on Gd atom according to the mGM3+ representation (Gd atom at the 2*c* Wyckoff position (*P*4/*nmm*). The (110) reflection at 4 K, within the AFM1 phase but slightly below AFM2, is nearly field-independent.

From the distribution of the magnetic intensities, one can make a first guess about the magnetic structure, assuming the most straightforward possibility, *i.e.,* single-*k* models. For an incommensurate magnetic structure described by a given *k*-vector, the magnetic moment at a given $\vec{r}$ (*x*, *y*, *z*) position is expressed through a general equation of a helical wave:

$$\vec{M} = \vec{M}_{\sin}\cdot\sin(2\pi\vec{k}\vec{r}) + \vec{M}_{\cos}\cdot\cos(2\pi\vec{k}\vec{r})$$

Here $\vec{M}_{sin}$, $\vec{M}_{cos}$ are orthogonal amplitudes. For our magnetic structures, these components are collected in the tables in Fig. 5 and Fig. 6. In the magnetically ordered crystals possessing a nontrivial symmetry, some of those components are constrained to zero, reducing the number of parameters to be determined from the experiment. The possible maximal magnetic superspace space groups (MSSG) can be constructed directly from the parent structural space group and the direction of the magnetic vector using representation analysis. The magnetic structures were solved and refined from the zero-field data collected for the small crystal in the Displex cryostat.

For k_I at 2 K, we collected 113 reflections. For 36 reflections, the intensities are above 3σ (for 43 reflections, above 2σ). k_I is located at the K(0 *b g*) point of the Brillouin Zone (BZ) with *b* = 0.45 and *g* = 0.45 in our case. This point has two possible irreducible representations (irreps.), mK_1 and mK_2. They correspond to maximal MSSG with one symmetry-independent Gd atom in the unit cell, $P2_1/m0.1'(a0g)00\,s$ (No. 11.1.2.1.m51.2, two variable components of the magnetic wave – M_{ysin}, M_{ycos}) $P2_1/m0.1'(a0g)0ss$ (No. 11.1.2.2.m51.2, four variable components of magnetic wave). Although the first one has just two parameters, it yields a better fit (R_F = 12.3 % and χ^2 = 2.6 *vs* R_F = 25.1 % and χ^2 = 6.9). The solution can be found among the subgroups of the $P2_1/m0.1'(ab0)00\,s$ MSSG. Removal of the *m*-plane leads to $P2_10.1'(a0g)0\,s$, which provides better residuals (R_F = 11.8 %, χ^2 = 1.9) while still having a single symmetrically independent Gd atom with all six variable components of the magnetic wave. As follows from the consequent refinement, the M_{zsin} and M_{zcos} components are zero, *i.e.,* the magnetic structure is planar. The parameters of the refined magnetic model are provided in Fig. 5, together with its schematic drawing. The F_{obs}-F_{cals} plot (provided in Fig. S6) shows a good agreement between the experimentally obtained structure factors and those calculated from our model. Most reflections fall within three standard deviations, whereas not-fully accountable absorption and extinction effects can probably explain the observed discrepancies. The magnetic moments of Gd atoms have a variable amplitude and lie in the *ab*-plane. The nearest members within the *ab*-plane are coupled nearly antiparallel; they rotate from one unit cell to another, forming a cycloid.

For k_{II}, we collected 24 reflections, 11 of which had intensities above 3σ (13 above 2σ). k_{II} is located at the DT(0 *b* 0) point of BZ with *b* = 0.4 in our case. This point has four irreps. The mDT_2 irrep with the highest symmetry solution in *Pmmn*.1'*(a*00*)0sss* MSSG, with two variable components of magnetic moment on Gd atom (M_{zsin} and M_{xcos}), provides the best fit (R_F = 22 % *vs.* 68 %, 25 % and 52 % for mDT_1, mDT_3, and mDT_4 respectively). From consequent testing of subgroups of this superspace group, one can find that adding the M_{ysin} component improves the fit. These three (and only them) variable components are allowed in $Pm2_1n.1'(a00)00ss$, which corresponds to removal of the m_y and m_y' planes from the maximal MSSG. Consequent refinement improves the residuals (R_F = 17 %, χ^2 = 3.4, Fig. S6) and yields a constant-moment ($|M|_{sin} = |M|_{cos}$) magnetic structure provided in Fig. 6. This structure is a cycloid. Magnetic moments of a constant amplitude rotate in the plane slightly tilted off the *ab*-plane.

3.4. General overview

We studied magnetic ordering in $GdSb_{0.71}Te_{1.22}$, which shows a complex phase diagram and CDW atomic superstructure. Two magnetic propagation vectors k_I = (0.45 0 0.45) and k_{II} = (0.4 0 0), that characterize the magnetic ordering at the base temperature, were identified. The ordering vector k_I in our crystal has two incommensurate components (along the *a*- or *b*-axis and along the *c*-axis). Its full star contains eight arms, namely ± (0.45 0 0.45), ± (0.45 0 −0.45), ± (0 0.45 0.45), and ± (0 0.45 −0.45), transformed into one another through the elements of the *P*4/*nmm* group, *i.e.* the symmetry of the paramagnetic state that is effectively observed in single-crystal measurements. As follows from high-resolution X-ray powder diffraction data, the real crystal symmetry is orthorhombic (*a*- and *b*-directions are not equivalent) whereas the tetragonal symmetry seemingly observed in single-crystal data is due to the ferroelastic structural twinning. We propose spin textures for the individual k_I and k_{II} vectors using (3D+1) MSSG, which provide nice fits. The k_I and k_{II} vectors correspond to different magnetic phases, *i.e.,* we deal with the phase separation scenario. The driving force of the transition at T_1 is formation of a constant-moment structure. The question remains if the k_I magnetic structure could possibly be

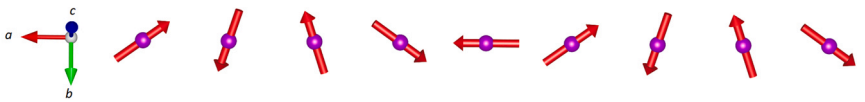

Gd	*x*	*y*	*z*
sin	0	1.2(2)	0.7(3)
cos	1.4(2)	0	0

Fig. 6.. Details of the magnetic structure corresponding to k_{II} – schematic representation of the structure and (*x, y, z*) components of the magnetic wave.

multi-*k* (multi-arm), within (3D+2) MSSGs, which predisposes non-trivial topology. The in-field scans of the magnetic Bragg peaks were not conclusive in this respect.

The components of the magnetic propagation vectors are very close to ½, *i.e.* one can write them as: k_I = (½ - δ_1 0 ½ - δ_2) and k_{II} = (½ - δ_3 0 0). Interestingly, this is in line with the fact that magnetic moments on the nearest atoms are aligned in an antiparallel manner along the *a*- and *c*-axes. This contrasts with the situation when the magnetic propagation vector is close to zero and the moment on the nearest atoms are aligned nearly parallel, like, for example, in CeAlGe [46]. The degree of deviation from the collinearity is related with δ, which defines the characteristic scale of the magnetic texture. Overall, the magnetic propagation vectors on their own hint at the possibility of non-collinear antiparallel-aligned spin textures.

Another way to rationalize this phenomenon is to compare the Gd member with the other *Ln*SbTe compounds we studied before [47]. HoSbTe and TbSbTe have qualitatively similar behavior: they order with the commensurate propagation vectors k_1 = (½ 0 0) and k_2 = (½ 0 ¼) at the lowest temperature, and with incommensurate propagation vectors k_1' = (½ - δ 0 0) and k_3 = (½ - δ 0 ½) at intermediate temperatures slightly below T_N. One can think about the commensurate vectors as harmonics of a "master propagation vector" *K* = (½ 0 g) with g = 0, ¼, and ½, while the incommensurate ones are just those subjected to small deviations from *K*. For the Ho and Tb members, the incommensurate vectors lock their components to commensurate values when approaching the base temperature. One origin of this lock-in is probably in the single-ion anisotropy. For the Gd member, the anisotropy is small (due to the absence of the orbital component in the half-filled 4*f* shell); this allows the propagation vectors to persist in being incommensurate (for g = ½, k_I = (½ – δ 0 ½ – δ), for g = 0, k_{II} = (½ – δ 0 0)) down to the base temperature. Multi-*k* magnetic ordering has been observed in TbSbTe [47], which may hint at a similar scenario in $GdSb_{0.71}Te_{1.22}$.

Finally, although we were not able to test the effect of the magnetic field on the behavior of the superstructure CDW satellites, the absence of effects in the temperature dependence of their intensities together with the absence of significant features in ADP curves for the (Sb/Te) and Te positions (unlike for Gd) indicates the magnetic and non-magnetic subsystems to be likely disentangled. This is rationalized by the fact that the Peierls-distortion-driven corrugations in the (Sb/Te) mixed square-net layer are, in fact, of the order of only 0.05 Å, which is most likely insufficient to perturb the magnetic exchanges. And *vice versa*, the magnetic ordering at low temperatures causes too little strain to affect the geometry of the non-magnetic part.

4. Conclusions

The antiferromagnetic skyrmion candidate $GdSb_{0.71}Te_{1.22}$ has been elucidated through magnetization measurements, single-crystal and powder X-ray diffraction as well as hot neutron single-crystal diffraction. The initial small orthorhombic unit cell already at room temperature features a long-periodicity nuclear superstructure due to the wave-like displacement of atoms. Below T_N = 11.9 K, the compound undergoes several magnetic transitions. At the base temperature, the magnetic ordering is characterized by two incommensurate propagation vectors k_I = (0.45 0 0.45) and k_{II} = (0.4 0 0). These vectors, having their components close to ½, might predispose long-wavelength non-collinear magnetic textures with the nearly antiparallel magnetic moments on the nearest atoms. Although we did not find the direct evidence of multi-*k* magnetic ordering, predisposing the non-trivial topology and skyrmion state, we show that our diffraction data do not exclude this possibility, and discuss the scenario, which can lead to such state.

CRediT authorship contribution statement

Igor Plokhikh: Conceptualization, Formal analysis, Investigation, Visualization, Writing – original draft. **Oscar Fabelo:** Investigation, Software, Data curation, Resources, Writing – review & editing. **Lilian Prodan:** Investigation, Writing – review & editing. **Michael Wörle:** Investigation, Resources, Writing – review & editing. **Ekaterina Pomjakushina:** Resources, Validation, Writing – review & editing. **Antonio Cervellino:** Investigation, Resources, Writing – review & editing. **Vladimir Tsurkan:** Investigation, Conceptualization, Writing – review & editing. **István Kézsmárki:** Supervision, Resources, Writing – review & editing. **Oksana Zaharko:** Supervision, Project administration, Funding acquisition, Methodology, Conceptualization.

Data Availability

Data will be made available on request.

Declaration of Competing Interest

The authors declare that they have no known competing financial interests or personal relationships that could have appeared to influence the work reported in this paper.

Acknowledgements

We acknowledge the Institut Laue-Langevin in Grenoble (France) for beam time allocation. We thank the Swiss National Science Foundation (grants No. 200020-182536/1 and 200021_188706) and SNI Swiss Nanoscience Institute for financial support. This work was partially supported by the Deutsche Forschungsgemeinschaft (DFG) through Transregional Research Collaboration TRR 80 (Augsburg, Munich, and Stuttgart) and *via* the DFG Priority Program SPP2137, Skyrmionics, under Grant No. KE 2370/1-1, and by the project ANCD 20.80009.5007.19 (Moldova).

Appendix A. Supporting information

Supplementary data associated with this article can be found in the online version at doi:10.1016/j.jallcom.2022.168348.

References

[1] M.Z. Hasan, C.L. Kane, Colloquium: topological insulators, Rev. Mod. Phys. 82 (2010) 3045, https://doi.org/10.1103/RevModPhys.82.3045
[2] A.A. Burkov, Weyl metals, Annu. Rev. Condens. Matter Phys. 9 (2018) 359, https://doi.org/10.1146/annurev-conmatphys-033117-054129
[3] B. Yan, C. Felser, Topological materials: weyl semimetals, Annu. Rev. Condens. Matter Phys. 8 (2017) 337, https://doi.org/10.1146/annurev-conmatphys-031016-025458
[4] S. Muhlbauer, B. Binz, F. Jonietz, C. Pfleiderer, A. Rosch, A. Neubauer, R. Georgii, P. Boni, Skyrmion lattice in a chiral magnet, Science 323 (2009) 915, https://doi.org/10.1126/science.1166767
[5] X.Z. Yu, Y. Onose, N. Kanazawa, J.H. Park, J.H. Han, Y. Matsui, N. Nagaosa, Y. Tokura, Real-space observation of a two-dimensional skyrmion crystal, Nature 465 (2010) 901, https://doi.org/10.1038/nature09124
[6] N. Nagaosa, Y. Tokura, Topological properties and dynamics of magnetic skyrmions, Nat. Nanotechnol. 8 (2013) 899, https://doi.org/10.1038/nnano.2013.243
[7] A. Fert, N. Reyren, V. Cros, Magnetic skyrmions: advances in physics and potential applications, Nat. Rev. Mater. 2 (2017) 17031, https://doi.org/10.1038/natrevmats.2017.31
[8] V. Baltz, A. Manchon, M. Tsoi, T. Moriyama, T. Ono, Y. Tserkovnyak, Antiferromagnetic spintronics, Rev. Mod. Phys. 90 (2018) 015005, https://doi.org/10.1103/RevModPhys.90.015005
[9] M. Hervé, B. Dupé, R. Lopes, M. Böttcher, M.D. Martins, T. Balashov, L. Gerhard, J. Sinova, W. Wulfhekel, Nat. Commun. 9 (2018) 1015, https://doi.org/10.1038/s41467-018-03240-w
[10] A.O. Leonov, I. Kézsmárki, Skyrmion robustness in noncentrosymmetric magnets with axial symmetry: the role of anisotropy and tilted magnetic fields, Phys. Rev. B 96 (2017) 214413, https://doi.org/10.1103/PhysRevB.96.214413

[11] J.A.M. Paddison, G. Ehlers, A.B. Cairns, J.S. Gardner, O.A. Petrenko, N.P. Butch, D.D. Khalyavin, P. Manuel, H.E. Fischer, H. Zhou, A.L. Goodwin, J.R. Stewart, Suppressed-moment 2-*k* order in the canonical frustrated antiferromagnet $Gd_2Ti_2O_7$, npj Quantum Mater. 6 (2021) 99, https://doi.org/10.1038/s41535-021-00391-w

[12] T. Okubo, S. Chung, H. Kawamura, Multiple-*q* states and the skyrmion lattice of the triangular-lattice Heisenberg antiferromagnet under magnetic fields, Phys. Rev. Lett. 108 (2012) 017206, https://doi.org/10.1103/PhysRevLett.108.017206

[13] S. Gao, H.D. Rosales, F.A.G. Albarracín, V. Tsurkan, G. Kaur, T. Fennell, P. Steffens, M. Boehm, P. Čermák, A. Schneidewind, E. Ressouche, D.C. Cabra, C. Rüegg, O. Zaharko, Fractional antiferromagnetic skyrmion lattice induced by anisotropic couplings, Nature 586 (2020) 37, https://doi.org/10.1038/s41586-020-2716-8

[14] Y. Yasui, C.J. Butler, N.D. Khanh, Imaging the coupling between itinerant electrons and localised moments in the centrosymmetric skyrmion magnet $GdRu_2Si_2$, Nat. Commun. 11 (2020) 5925, https://doi.org/10.1038/s41467-020-19751-4

[15] M. Hirschberger, T. Nakajima, M. Kriener, T. Kurumaji, L. Spitz, S. Gao, A. Kikkawa, Y. Yamasaki, H. Sagayama, H. Nakao, S. Ohira-Kawamura, Y. Taguchi, T. Arima, Y. Tokura, High-field depinned phase and planar Hall effect in the skyrmion host Gd_2PdSi_3 (R), Phys. Rev. B 101 (2020) 220401, https://doi.org/10.1103/PhysRevLett.125.076602

[16] T. Xu, Z. Chen, H. Zhou, Z. Wang, Y. Dong, L. Aballe, M. Foerster, P. Gargiani, M. Valvidares, D.M. Bracher, T. Savchenko, A. Kleibert, R. Tomasello, G. Finocchio, S. Je, M. Im, D.A. Muller, W. Jiang, Imaging the spin chirality of ferrimagnetic Néel skyrmions stabilized on topological antiferromagnetic Mn_3Sn, Phys. Rev. Mater. 5 (2021) 084406, https://doi.org/10.1103/PhysRevMaterials.5.084406

[17] C. Pappas, E. Lelièvre-Berna, P. Falus, P.M. Bentley, E. Moskvin, S. Grigoriev, P. Fouquet, B. Farago, Chiral Paramagnetic Skyrmion-like Phase in MnSi, Phys. Rev. Lett. 102 (2009) 197202, https://doi.org/10.1103/PhysRevLett.102.197202

[18] S. Gao, O. Zaharko, V. Tsurkan, Y. Su, J.S. White, G.S. Tucker, B. Roessli, F. Bourdarot, R. Sibille, D. Chernyshov, T. Fennell, A. Loidl, C. Rüegg, Spiral spin-liquid and the emergence of a vortex-like state in $MnSc_2S_4$, Nat. Phys. 13 (2017) 157, https://doi.org/10.1038/nphys3914

[19] S. Lei, A. Saltzman, L.M. Schoop, Complex magnetic phases enriched by charge density waves in the topological semimetals $GdSb_xTe_{2-x-\delta}$, Phys. Rev. B 103 (2021) 134418, https://doi.org/10.1103/PhysRevB.103.134418

[20] M. Neupane, I. Belopolski, M.M. Hosen, D.S. Sanchez, R. Sankar, M. Szlawska, S.-Y. Xu, K. Dimitri, N. Dhakal, P. Maldonado, P.M. Oppeneer, D. Kaczorowski, F. Chou, M.Z. Hasan, T. Durakiewicz, Observation of topological nodal fermion semimetal phase in ZrSiS, Phys. Rev. B 93 (2016) 201104, https://doi.org/10.1103/PhysRevB.93.201104

[21] L.M. Schoop, M.N. Ali, C. Straßer, A. Topp, A. Varykhalov, D. Marchenko, C.R. Ast, Dirac cone protected by non-symmorphic symmetry and three-dimensional Dirac line node in ZrSiS, Nat. Commun. 7 (2016) 1, https://doi.org/10.1038/ncomms11696

[22] Y. Wang, Y. Qian, M. Yang, H. Chen, C. Li, Z. Tan, Y. Cai, W. Zhao, S. Gao, Y. Feng, S. Kumar, E.F. Schwier, L. Zhao, H. Weng, Y. Shi, G. Wang, Y. Song, Y. Huang, K. Shimada, Z. Xu, X.J. Zhou, G. Liu, Spectroscopic evidence for the realization of a genuine topological nodal-line semimetal in LaSbTe, Phys. Rev. B 103 (2021) 125131, https://doi.org/10.1103/PhysRevB.103.125131

[23] M. Yang, Y. Qian, D. Yan, Y. Li, Y. Song, Z. Wang, C. Yi, H.L. Feng, H. Weng, Y. Shi, Magnetic and electronic properties of a topological nodal line semimetal candidate: HoSbTe, Phys. Rev. Mater. 4 (2020) 094203, https://doi.org/10.1103/PhysRevMaterials.4.094203

[24] S. Regmi, G. Dhakal, F.C. Kabeer, N. Harrison, F. Kabir, A. Pradhan Sakhya, K. Gofryk, D. Kaczorowski, P.M. Oppeneer, M. Neupane, Observation of multiple nodal-lines in SmSbTe, Phys. Rev. Mater. 6 (2022) L031201, https://doi.org/10.1103/PhysRevMaterials.6.L031201

[25] L.M. Schoop, A. Topp, J. Lippmann, F. Orlandi, L. Müchler, M.G. Vergniory, B.V. Lotsch, Tunable Weyl and Dirac states in the nonsymmorphic compound CeSbTe, Sci. Adv. 4 (2018) eaar2317, https://doi.org/10.1126/sciadv.aar2317

[26] R. Singha, T.H. Salters, S.M. Teicher, S. Lei, J.F. Khoury, N.P. Ong, L.M. Schoop, Evolving Devil's staircase magnetization from tunable charge density waves in nonsymmorphic Dirac semimetals, Adv. Mater. 33 (2021) 2103476, https://doi.org/10.1002/adma.202103476

[27] M.M. Hosen, G. Dhakal, K. Dimitri, P. Maldonado, A. Aperis, F. Kabir, M. Neupane, Discovery of topological nodal-line fermionic phase in a magnetic material GdSbTe, Sci. Rep. 8 (2018) 1, https://doi.org/10.1038/s41598-018-31296-7

[28] S. Lei, S.M. Teicher, A. Topp, K. Cai, J. Lin, G. Cheng, L.M. Schoop, Band engineering of Dirac semimetals using charge density waves, Adv. Mater. (2021) 2101591, https://doi.org/10.1002/adma.202101591

[29] R. Sankar, I.P. Muthuselvam, K.R. Babu, G.S. Murugan, K. Rajagopal, R. Kumar, T.-C. Wu, C.-Y. Wen, W.-L. Lee, G.-Y. Guo, F.C. Chou, Crystal growth and magnetic properties of topological nodal-line semimetal GdSbTe with antiferromagnetic spin ordering, Inorg. Chem. 58 (2019) 11730, https://doi.org/10.1021/acs.inorgchem.9b01698

[30] G. Leinweber, D.P. Barry, M.J. Trbovich, J.A. Burke, N.J. Drindak, H.D. Knox, R.V. Ballad, R.C. Block, Y. Danon, L.I. Severnyak, Neutron capture and total cross-section measurements and resonance parameters of gadolinium, Nucl. Sci. Eng. 154 (2017) 261, https://doi.org/10.13182/NSE05-64

[31] D9 instrument web-page: ⟨www.ill.eu/users/instruments/instruments-list/d9/description/instrument-layout⟩.

[32] M.S. Lehmann, F.K. Larsen, A method for location of the peaks in step-scan measured Bragg reflexions, Acta Cryst. A. 30 (1974) 580, https://doi.org/10.1107/S0567739474001379

[33] N.A. Katcho, L. Cañadillas-Delgado, O. Fabelo, M.-T. Fernández-Díaz, J. Rodríguez-Carvajal, Int3D: a data reduction software for single crystal neutron diffraction, Crystals 11 (8) (2021) 897, https://doi.org/10.3390/cryst11080897

[34] I. Plokhikh, O. Fabelo, I. Kezsmarki, V. Tsurkan, O. Zaharko, Search for topological magnetic order in $GdSb_xTe_{2-x}$ square-net antiferromagnet, Inst. Laue-Lange (ILL) (2021), https://doi.org/10.5291/ILL-DATA.DIR-255

[35] P.R. Willmott, D. Meister, S.J. Leake, M. Lange, A. Bergamaschi, M. Böge, M. Calvi, C. Cancellieri, N. Casati, A. Cervellino, Q. Chen, C. David, U. Flechsig, F. Gozzo, B. Henrich, S. Jäggi-Spielmann, B. Jakob, I. Kalichava, P. Karvinen, J. Krempasky, A. Lüdeke, R. Lüscher, S. Maag, C. Quitmann, M.L. Reinle-Schmitt, T. Schmidt, B. Schmitt, A. Streun, I. Vartiainen, M. Vitins, X. Wang, R. Wullschleger, The Materials Science beamline upgrade at the Swiss Light Source, J. Synchrotron Rad. 20 (2013) 667, https://doi.org/10.1107/S0909049513018475

[36] Agilent, CrysAlis PRO, Agilent Technologies Ltd, Yarnton, Oxfordshire, England, 2014.

[37] V. Petricek, M. Dusek, L. Palatinus, Crystallographic computing system JANA2006: general features, Z. Krist. 229 (2014) 345, https://doi.org/10.1515/zkri-2014-1737

[38] Vaclav Petricek, Michal Dusek, Lukas Palatinus, jana.fzu.cz.

[39] J.M. Perez-Mato, J.L. Ribeiro, V. Petricek, M.I. Aroyo, Magnetic superspace groups and symmetry constraints in incommensurate magnetic phases, J. Condens. Matter Phys. 24 (2012) 163201, https://doi.org/10.1088/0953-8984/24/16/163201

[40] H.T. Stokes, D.M. Hatch, B.J. Campbell, ISODISTORT, ISOTROPY Software Suite, iso.byu.edu.

[41] B.J. Campbell, H.T. Stokes, D.E. Tanner, D.M. Hatch, ISODISPLACE: an internet tool for exploring structural distortions, J. Appl. Cryst. 39 (2006) 607, https://doi.org/10.1107/S0021889806014075

[42] K. Momma, F. Izumi, VESTA 3 for three-dimensional visualization of crystal, volumetric and morphology data, J. Appl. Cryst. 44 (2011) 1272, https://doi.org/10.1107/S0021889811038970

[43] Neutron scattering lengths and cross sections ⟨www.ncnr.nist.gov/resources/n-lengths/⟩.

[44] E.S. Nikova, Y.A. Salamatov, E.A. Kravtsov, V.I. Bodnarchuk, V.V. Ustinov, Experimental determination of gadolinium scattering characteristics in neutron reflectometry with reference layer, Phys. B: Condens. Matter 552 (2019) 58–61, https://doi.org/10.1016/j.physb.2018.09.033

[45] J.E. Lynn, P.A. Seeger, Resonance effects in neutron scattering lengths of rare-earth nuclides, At. Data Nucl. Data Tables 44 (1990) 191, https://doi.org/10.1016/0092-640X(90)90013-A

[46] P. Puphal, V. Pomjakushin, N. Kanazawa, V. Ukleev, D.J. Gawryluk, J. Ma, M. Naamneh, N.C. Plumb, L. Keller, R. Cubitt, E. Pomjakushina, J.S. White, Topological magnetic phase in the candidate weyl semimetal CeAlGe, Phys. Rev. Lett. 124 (2020) 017202, https://doi.org/10.1103/PhysRevLett.124.017202

[47] I. Plokhikh, V. Pomjakushin, D.J. Gawryluk, O. Zaharko, E. Pomjakushina., Competing magnetic phases in *Ln*SbTe (*Ln* = Ho and Tb), Inorg. Chem. 61 (2022) 11399–11409, https://doi.org/10.1021/acs.inorgchem.2c01711